Dalton Transactions

ROYAL SOCIETY OF CHEMISTRY

PAPER

View Article Online
View Journal

Cite this: DOI: 10.1039/d0dt03083j

Direct structural and mechanistic insights into fast bimolecular chemical reactions in solution through a coupled XAS/UV–Vis multivariate statistical analysis†

Francesco Tavani,*[a] Giorgio Capocasa,[a] Andrea Martini,[b,c] Francesco Sessa, [a] Stefano Di Stefano, [a] Osvaldo Lanzalunga [a] and Paola D'Angelo [a]*

Received 3rd September 2020,
Accepted 25th November 2020

DOI: 10.1039/d0dt03083j

rsc.li/dalton

In this work, we obtain detailed mechanistic and structural information on bimolecular chemical reactions occurring in solution on the second to millisecond time scales through the combination of a statistical, multivariate and theoretical analysis of time-resolved coupled X-ray Absorption Spectroscopy (XAS) and UV–Vis data. We apply this innovative method to investigate the sulfoxidation of *p*-cyanothioanisole and *p*-methoxythioanisole by the nonheme Fe^{IV} oxo complex $[N4Py{\cdot}Fe^{IV}(O)]^{2+}$ (N4Py = *N*,*N*-bis(2-pyridylmethyl)-*N*-bis(2-pyridyl)methylamine) in acetonitrile at room temperature. By employing statistical and multivariate techniques we determine the number of key chemical species involved along the reaction paths and derive spectral and concentration profiles for the reaction intermediates. From the quantitative analysis of the XAS spectra we obtain accurate structural information for all reaction intermediates and provide the first structural characterization in solution of complex $[N4Py{\cdot}Fe^{III}(OH)]^{2+}$. The employed strategy is promising for the spectroscopic characterization of transient species formed in redox reactions.

1. Introduction

Synergistic and interdisciplinary efforts are required to strengthen the comprehension of chemical reactivity. In fact, the increasing complexity of the systems investigated by modern researchers makes it necessary to extend the tools available for the elucidation of reaction mechanisms and for the structural characterization of their transient intermediates that are frequently silent to conventional experimental methods of detection. Indeed, the accurate understanding of the elementary steps that from reactants lead to products should allow one to address previously unsolved mechanistic controversies and to access the structures of the reaction key species, whose knowledge is essential to comprehensively describe a given transformation.

In this work, we present an innovative method to study the mechanisms of bimolecular chemical reactions occurring in solution on the second to millisecond time scales and to characterize the structures of their relevant chemical intermediates. The employed approach combines a statistical, multivariate and theoretical analysis of time-resolved coupled Energy Dispersive X-ray Absorption Spectroscopy (EDXAS)/UV–Vis data. Within this framework, we apply to the coupled EDXAS/UV–Vis experimental spectra a method that integrates Principal Component Analysis (PCA) and a strategy belonging to the Multivariate Curve Resolution (MCR) family to decompose the measured signals in a set of N uncorrelated spectra, associated to the reaction key components, and in the set of their relative concentrations, following the Lambert–Beer law. The extracted concentration profiles are then used for a mechanistic analysis of the investigated processes. Finally, quantitative information on the molecular geometry of all reaction intermediates is gained by theoretical X-ray Absorption Near Edge Structure (XANES) simulations.

MCR methods have been extensively employed to extract qualitative and quantitative information from the spectroscopic monitoring of chemical processes, using, for instance, UV–Vis,[1–4] fluorescence,[5–7] nuclear magnetic resonance,[8–10] circular dichroism,[11,12] near-infrared (NIR),[13–15] Fourier Transform IR (FTIR),[16–18] time-resolved FTIR,[19–21] and Raman spectroscopy.[22,23] Among these conventional experimental approaches, X-ray absorption spectroscopy (XAS) stands out as an advanced technique that is being increasingly applied to

[a]*Dipartimento di Chimica, Università di Roma "La Sapienza", P.le A. Moro 5, 00185 Roma, Italy. E-mail: p.dangelo@uniroma1.it, francesco.tavani@uniroma1.it*
[b]*Dipartimento di Chimica, Università degli Studi di Torino, Via P. Giuria 7, 10125 Torino, Italy*
[c]*The Smart Materials Research Institute, Southern Federal University, 344090 Sladkova178/24 Rostov-on-Don, Russia*

†Electronic supplementary information (ESI) available. See DOI: 10.1039/D0DT03083J

follow chemical reactions involving organic substrates.[24–26] XAS offers, in fact, some important and unique advantages: the capability of following both the electronic and structural variation in configuration around a certain photoabsorbing atom,[27] and the possibility to extract structural insight by reproducing the experimental spectra with theoretical simulations of growing reliability. For instance, we have recently used EDXAS in combination with UV–Vis spectroscopy to identify the sequence of oxidation states in bimolecular reactions occurring in solution on second to millisecond timescales and to measure reliable pseudo-first order kinetic constants.[28,29]

The application of PCA to XANES time-resolved data relative to chemical reactions has been widespread, while that of MCR is a relatively new development. Frenkel *et al.* employed PCA together with multiple data set fits of the Extended X-ray Absorption Fine Structure (EXAFS) region and the residual phase analysis,[30] a method employed as well to investigate biochemical processes.[31,32] An additional method relying on PCA and on the assumption that at a certain time the percentage of the intermediate state is 100% was proven to be successful for the analysis of the reduction and reoxidation of Cu-doped ceria catalysts.[33] Further, the joint use of PCA with a XANES multidimensional interpolation approach was applied to EDXAS data coming from a reaction involving a methylrhenium trioxide catalyst in solution. This strategy enabled the determination of the geometries and of the concentration time evolution pertaining to the reaction intermediates.[34] Conversely, the MCR algorithm is gaining increasing interest for the understanding of chemical transformations, with studies dedicated, for example, to ZnO Q-dot growth models,[35] phase speciation of chlorine under temperature-programmed transformation,[36] Cu speciation and reducibility in Cu–CHA zeolite catalysts,[37,38] and other systems so far mainly in the solid phase.[39–44] By combining the analyses of both EDXAS and UV–Vis spectroscopic data, herein we develop an approach that allows one to greatly reduce the non-uniqueness of the extracted solutions to the decomposition problem, thereby limiting the rotational ambiguity that affects the MCR methods which rely on a single set of spectroscopic measurements.[45,46]

Oxygen atom transfer (OAT) to organic and inorganic substrates may be promoted by high-valent metal–oxo species with heme and nonheme ligands formed in heme and nonheme iron oxygenases and their synthetic counterparts.[47,48] OAT is a key step in numerous biological and catalytic reactions and its mechanism has been widely investigated.[49–51] Two distinct pathways have been proposed for sulfoxidation reactions catalyzed by high-valent metal–oxo complexes: a direct oxygen transfer (DOT) and an electron transfer preceding an oxygen transfer (ET-OT).[48,52–54] This mechanistic dichotomy has been recently investigated in detail for the oxidation of aromatic sulfides promoted by $[N4Py{\cdot}Fe^{IV}(O)]^{2+}$ (N4Py = *N*,*N*-bis(2-pyridylmethyl)-*N*-bis(2-pyridyl)methylamine), that oxidizes *para*-X substituted thioanisoles (where X = CH_3, H, Cl, CN) through a DOT process in the presence of perchloric acid or without acid additives.[47,55] Conversely, if the same reactions are performed in the presence of $Sc(OTf)_3$ or triflic acid a metal ion-coupled ET and a proton-coupled ET have been shown to occur, respectively, prior to the OT.[56,57] The switch to the ET-OT process was made clear in the reaction of $[N4Py{\cdot}Fe^{IV}(O)]^{2+}$ (1.0×10^{-3} M) with *p*-methoxythioanisole (4.0×10^{-3} M) in the presence of Sc^{3+} (4.0×10^{-3} M), by the transitory appearance at 580 nm of the UV–Vis absorption signal associated to the *p*-methoxythioanisole radical cation formed after the initial ET step.[47] Additional substrates, such as aryl-1-methyl-1-phenylethyl and aryl diphenylmethyl sulfides, are also known to be oxidized by $[N4Py{\cdot}Fe^{IV}(O)]^{2+}$ with an ET-OT mechanism as demonstrated by the observation of fragmentation products deriving from C–S bond cleavage of the corresponding aryl sulfide radical cations.[58–62]

Herein, we show the potential of our approach by investigating the sulfoxidation of two differently *para*-substituted thioanisoles, *p*-cyanothioanisole and *p*-methoxythioanisole, by the nonheme Fe^{IV} oxo complex $[N4Py{\cdot}Fe^{IV}(O)]^{2+}$, with the twofold aim of shedding light onto the reaction mechanisms and determining the structure of the elusive intermediates that are formed during the reaction pathways. The successful application of our methodology may provide a new tool to gain a comprehensive structural, mechanistic and kinetic picture for reactions involving organic substrates and occurring in solution on the second to millisecond time scales, together with contributing to understand the reactivity of nonheme complexes.

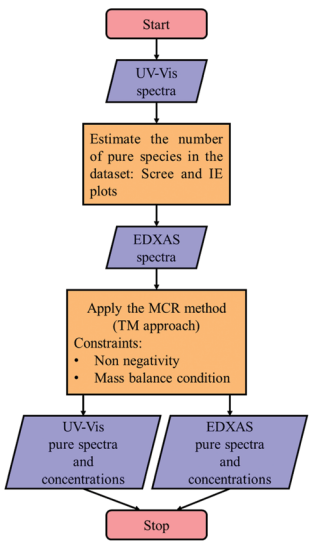

Fig. 1 Flow diagram reporting the procedure followed to decompose the UV–Vis and the EDXAS data sets relative to the oxidation of *p*-$CNC_6H_4SCH_3$ and of *p*-$CH_3OC_6H_4SCH_3$ by $[N4Py{\cdot}Fe^{IV}(O)]^{2+}$. Starting from the UV–Vis data, the number of chemical species contributing to the series of spectra is estimated by analyzing the Scree and the Imbedded Error (IE) function plots, respectively. The same number of species is supposed to characterise the EDXAS data set referring to the given reaction. Subsequently, the transformation matrix based MCR approach is applied to both data sets, allowing one to retrieve the spectral and concentration profiles of the pure species.

2. Results and discussion

The aim of our investigation is to address the need of new methods capable of shedding light onto chemical reactions whose previously proposed mechanisms are still controversial, also by accurately determining the three dimensional structure of the key reaction intermediates. Here, we present an innovative approach that combines theoretical and advanced experimental techniques which possess a structural and oxidation state sensitivity not accessible to other experimental procedures. The method was applied to evaluate the reactivity of *p*-cyanothioanisole (*p*-$CNC_6H_4SCH_3$) and of *p*-methoxythioanisole (*p*-$CH_3OC_6H_4SCH_3$) with the nonheme Fe^{IV} oxo complex $[N4Py{\cdot}Fe^{IV}(O)]^{2+}$, whose oxidations are slower and faster, respectively.[29] To this end, a multivariate statistical analysis was applied to the coupled EDXAS/UV–Vis data of both reactions as outlined in the flow-diagram reported in Fig. 1. In particular, the number N of chemical species present in the reaction mixtures is determined by applying two different statistical tests to the UV–Vis data sets, namely the Scree plot and the imbedded-error (IE) function test. The XAS and UV–Vis experimental data are then decomposed into the N spectral and concentration profiles belonging to the reaction intermediates using the transformation matrix (TM) MCR method implemented in the PyFitIt software (refer to the Method section of the ESI† for additional details).[45] Both reactions were carried out under pseudo-first-order conditions (*p*-$CNC_6H_4SCH_3$ 800 mM and *p*-$CH_3OC_6H_4SCH_3$ 100 mM, respectively, added to $[N4Py{\cdot}Fe^{IV}(O)]^{2+}$ 15 mM) in CH_3CN at 25 °C, with the iron–oxo complex pre-formed by reaction of the Fe^{II} complex $[N4Py{\cdot}Fe^{II}(CH_3CN)]^{2+}$ with peroxyacetic acid (220 mM, added as a 36–40% w/w AcOH stock solution).

Fig. 2 presents the UV–Vis time course of the reaction of $[N4Py{\cdot}Fe^{IV}(O)]^{2+}$ with *p*-$CNC_6H_4SCH_3$ followed through the absorbance decrease due to the decay of $[N4Py{\cdot}Fe^{IV}(O)]^{2+}$ (λ = 695 nm) and the absorbance increase due to the formation of $[N4Py{\cdot}Fe^{II}(CH_3CN)]^{2+}$ (λ = 513 nm). The presence of the isosbestic point in Fig. 2b (left panel, inset) suggests the direct interconversion of the Fe^{IV} species to the Fe^{II} state with no intermediate involved. Conversely, Fig. 3 presents the UV–Vis spectra recorded during the reaction of the nonheme Fe^{IV} oxo complex and *p*-$CH_3OC_6H_4SCH_3$. The absence of an isosbestic

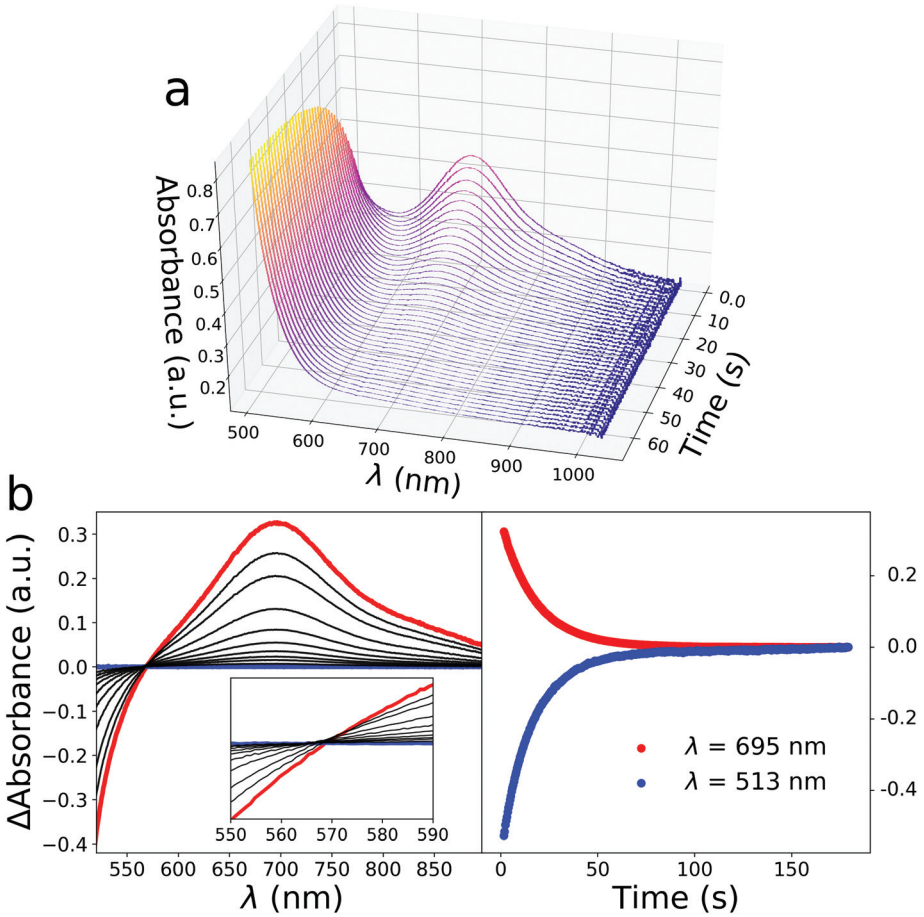

Fig. 2 UV–Vis monitoring of the reaction of $[N4Py{\cdot}Fe^{IV}(O)]^{2+}$ (15 mM) with *p*-$CNC_6H_4SCH_3$ (800 mM) in CH_3CN at 25 °C. (a) Time evolution of selected UV–Vis spectra from reaction start. (b) Changes in the UV–Vis spectra with a magnification of the spectral region between λ = 550 nm and λ = 590 nm (left panel) and time course monitoring at λ = 695 nm and λ = 513 nm (right panel). The first and last difference UV–Vis reaction spectra are highlighted in red and blue, respectively (left panel).

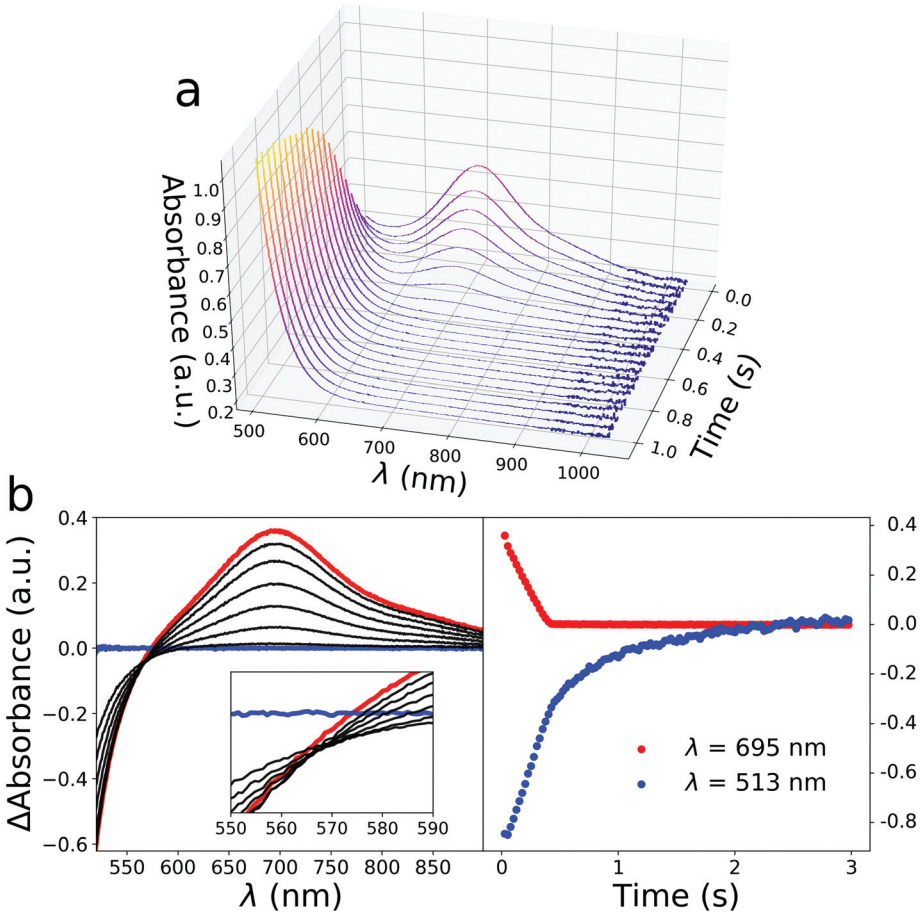

Fig. 3 UV–Vis monitoring of the reaction of $[N4Py{\cdot}Fe^{IV}(O)]^{2+}$ (15 mM) with *p*-$CH_3OC_6H_4SCH_3$ (100 mM) in CH_3CN at 25 °C. (a) Time evolution of selected UV–Vis spectra from reaction start. (b) Changes in the UV–Vis spectra with a magnification of the spectral region between λ = 550 nm and λ = 590 nm (left panel) and time course monitoring at λ = 695 nm and λ = 513 nm (right panel). The first and last difference UV–Vis reaction spectra are highlighted in red and blue, respectively (left panel).

point and the sharp absorbance decrease at λ = 695 nm compared to the slower corresponding increase at λ = 513 nm are indicative of the possible presence of a third, intermediate species. It is instructive to note that the absorbance time evolution at λ = 695 nm closely resembles the previously reported absorbance evolution at λ = 695 nm for the reaction of *p*-$CH_3OC_6H_4SCH_3$ and $[N4Py{\cdot}Fe^{IV}(O)]^{2+}$ in the presence of Sc^{3+}.[47]

In order to gain a quantitative insight into the number of pure chemical species contributing to the overall UV–Vis signals, the spectroscopic data were subjected to a statistical analysis as previously mentioned. In the Scree plot, the singular values associated to each principal component (PC) extracted through the Singular Value Decomposition (SVD) procedure are analyzed and plotted *versus* the number of components characterizing the data set (see Fig. 4). The identification of an elbow in the resulting curve marks the distinction between signal and noise related components. As for the reaction involving *p*-$CNC_6H_4SCH_3$, one may see in Fig. 4a that after the second component the intensities of the singular values rapidly drop down towards an approximately flat line. On the other hand, the Scree plot analysis for the *p*-$CH_3OC_6H_4SCH_3$ reaction (Fig. 4c) reveals that the third PC contributes non-negligibly to the experimental data, while starting from the fourth PC all components are associated to noise.

As detailed in the ESI,† given a number h of PCs employed to represent the experimental data matrix, it can be shown that the IE-function decreases for $h < N$ and increases for $h > N$ as a function of the number of PCs. It follows that the IE-function is minimized by the number of relevant components contributing to the overall signal. Fig. 4b and d show the IE-function test results for the UV–Vis data and the IE-function is minimized by N = 2 and N = 3 for the *p*-$CNC_6H_4SCH_3$ and *p*-$CH_3OC_6H_4SCH_3$ reactions, respectively. These findings are in good agreement with the Scree plot analysis, suggesting that while in the case of the *p*-$CNC_6H_4SCH_3$ reaction there are only two active species, namely the Fe^{IV} reactant and Fe^{II} product, in the case of *p*-$CH_3OC_6H_4SCH_3$ a third species contributes to the experimental UV–Vis data.

In order to obtain further insights into the mechanisms in place for the two processes, the UV–Vis data were decomposed in a set of spectral and concentration profiles referring to the

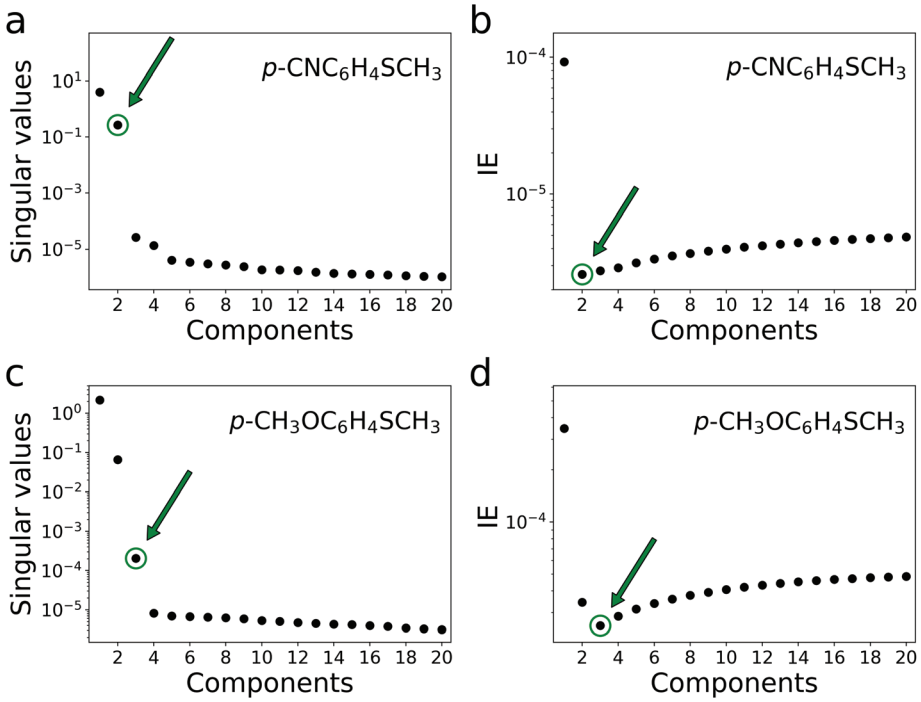

Fig. 4 Statistical analysis results. Scree plot and IE-function test for the UV–Vis reaction spectra involving p-$CNC_6H_4SCH_3$ (panels (a) and (b), respectively) and p-$CH_3OC_6H_4SCH_3$ (panels (c) and (d), respectively). A green arrow indicates the number of principal components necessary to reproduce the UV–Vis data set suggested by each statistical test.

reaction components. Fig. 5a and b show the isolated UV-Vis spectra and fractional concentrational profiles for the p-$CNC_6H_4SCH_3$ reaction. The first spectrum (red) belongs to complex $[N4Py{\cdot}Fe^{IV}(O)]^{2+}$, exhibiting an absorbance maximum at λ = 695 nm, while the second spectrum (blue) is assigned to complex $[N4Py{\cdot}Fe^{II}(CH_3CN)]^{2+}$. The extracted spectra are in excellent agreement with the known spectra for the two species, shown in Fig. S2.† The exponential fit of both concentration profiles provides a pseudo-first-order kinetic constant k = 0.052 ± 0.002 s^{-1} (Fig. S3†). This value is slightly higher than that reported in the literature,[63] a result that can be rationalized on the basis of the higher reactivity of the Fe^{IV} oxo complex induced by the acid medium (*vide infra*).

At this point, one can use the relative concentrations acquired by means of the UV–Vis data decomposition as mathematical constraints for the analysis of the EDXAS p-$CNC_6H_4SCH_3$ reaction spectra (previously subjected to a smoothing procedure using the Savitzky–Golay filter)[64] shown as a continuous evolution in Fig. S1a.† This procedure allows one to recover the XANES spectra associated to the species present in the reaction mixture. According to the Lambert and Beer law,[45] it is possible to assert that each EDXAS spectrum, constituting the experimental data set, can be written as the linear combination of the two spectra, corresponding to the identified reaction components and weighted by their relative concentrations. It follows that the experimental EDXAS data set D can be expressed as:

$$D = S \cdot C + E \quad (1)$$

where every column of D is an EDXAS experimental spectrum while matrices S and C contain respectively, on their columns and rows, the EDXAS spectra and concentration profiles referring to the two reaction key species. Finally E is a matrix of residuals depending on the chemical species involved in the data mixture.[65] Because the concentration matrix C has been retrieved from the UV–Vis data set shown in Fig. 5b, it can be properly employed in the classical least squares method to recover matrix S as:

$$S = D \cdot C^{T} \cdot (C \cdot C^{T})^{-1} \quad (2)$$

where the letter T denotes the transpose operator. The set of spectral profiles S given by eqn (2) are refined in order to minimize the residuals E of eqn (1). Fig. 5c shows the derived XANES spectra assigned to complex $[N4Py{\cdot}Fe^{IV}(O)]^{2+}$ (red) and to complex $[N4Py{\cdot}Fe^{II}(CH_3CN)]^{2+}$ (blue).

In order to determine the energy position of the Fe main absorption edges we have decomposed the threshold region of each spectrum as the sum of an arctangent function accounting for the transition into the continuum and a Lorentzian function due to the 1s → 4s transition, as shown in Fig. S4.† The oxidation state of each XANES spectrum is assigned by the energy position of the main absorption edge determined as that of the arctangent inflection point. These values are 7124.7 eV and 7126.2 eV for the Fe^{II} and Fe^{IV} complexes, respectively, and are listed in Table S1† together with the edge energy values of the same complexes previously determined.[66] The absolute energy difference between these last two values is

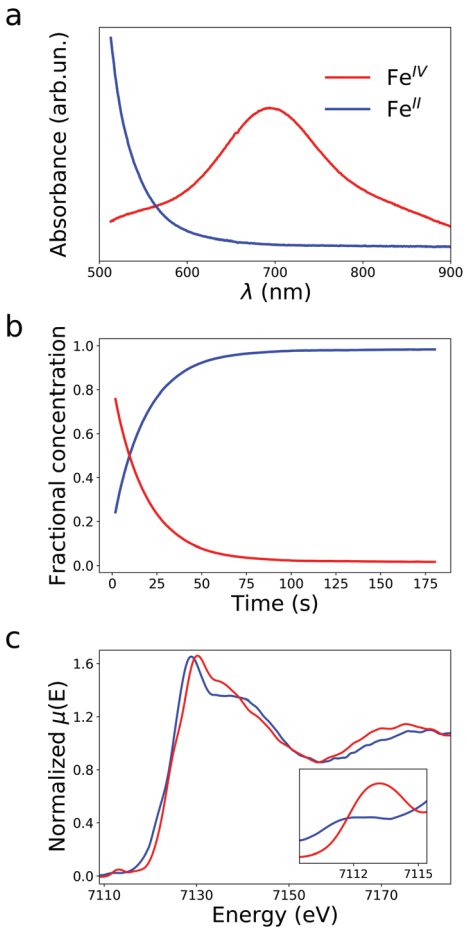

Fig. 5 UV–Vis spectra (a) and fractional concentration profiles (b) obtained through the matricial decomposition of the UV–Vis data for the *p*-$CNC_6H_4SCH_3$ oxidation. (c) Fe K-edge XANES spectra derived through matricial division and assigned to the two reaction key species. A magnification of the pre-edge region is shown in the inset.

1.7 eV, in good agreement with the absolute energy difference between the main absorption edges of the Fe^{IV} and Fe^{II} species that we report, which is equal to 1.5 eV. Interestingly, the Fe^{IV} species possesses an intense 1s → 3d dipole-forbidden transition located at 7113.3(2) eV. In fact, it is known that nonheme Fe^{IV} oxo complexes show relatively intense 1s → 3d transitions due to their non-centrosimmetry and it has been reported this is the case also for complex $[N4Py{\cdot}Fe^{IV}(O)]^{2+}$.[67,68] This same feature is very weak and centered at 7111.8(2) eV in the spectrum of the Fe^{II} complex (see inset in Fig. 5c. Previously, Rohde *et al.* reported pre-edge energies of 7114.3 eV and 7112.9 eV for the Fe^{IV} and Fe^{II} complexes, respectively, and that the transition area belonging to the Fe^{IV} species is approximately six times greater than that of $[N4Py{\cdot}Fe^{II}(CH_3CN)]^{2+}$.[66] In a following work, the pre-edge energies of a series of Fe^{II},[69] Fe^{III},[70] and Fe^{IV} complexes were uniformly re-assessed in order to eliminate ambiguities due to the differences in normalization and calibration procedures and a pre-edge energy of 7113.6 eV was reported for complex $[N4Py{\cdot}Fe^{IV}(O)]^{2+}$, a value in line with the one we have determined for the Fe^{IV} species.[71] If one were to apply the same energy shift of −0.7 eV to the literature pre-edge energy of $[N4Py{\cdot}Fe^{II}(CH_3CN)]^{2+}$, the estimated corrected value would be 7111.2 eV. This last value is coherent with the energy value of 7111.8(2) eV that we report for the pre-edge transition of the Fe^{II} species, and is also in good agreement with the pre-edge energies of other Fe^{II} high valent iron complexes such as, for example, $[Fe^{II}Cl_4]^{2-}$ and $[Fe^{II}Cl_4]^{4-}$ which are equal to 7112.1 eV and 7111.8 eV, respectively.[71] These findings further support the chemical identification of the two iron complexes.

Conversely, the results of the decomposition of the UV–Vis data relative to the *p*-$CH_3OC_6H_4SCH_3$ oxidation are shown in Fig. 6a. The first (red) and second (blue) spectrum belong to complexes $[N4Py{\cdot}Fe^{IV}(O)]^{2+}$ and $[N4Py{\cdot}Fe^{II}(CH_3CN)]^{2+}$, respectively. The third extracted spectral component (green), showing a very faint signal, is assigned to $[N4Py{\cdot}Fe^{III}(OH)]^{2+}$. In fact, it is known that the Fe^{III} complex exhibits a very weak, if any, absorbance in the spectral region of interest.[72,73] The fact that the MCR approach exploited in this work is able to identify a chemical species that has a very low UV–Vis signal is not surprising. The spectral decomposition procedure is based on the PCA of the collected set of experimental data, and it aims to identify algebraically a set of pure spectral profiles (having a chemical physical meaning) able to explain the highest variations in the data excluding the noise.[45,74] The presence of a pure, almost silent species clearly influences the system under study, causing an appreciable intensity variation of the experimental signal especially between 0.0 and 0.5 s. It is worth noting, in fact, that each experimental UV-Vis spectrum of the data set can be expressed as the linear combination of the three pure constituents provided by the MCR approach. It follows that the chemical species possessing the spectral contribution shown in Fig. 6a in green will provide the strongest contribution in the data set variance when its fraction will reach its maximum. The associated concentration profiles for the three reaction species, shown in Fig. 6b, support this hypothesis. The concentration of the Fe^{III} intermediate increases to reach a maximum before decaying to zero, while those of the Fe^{IV} initial species and Fe^{II} product decay and increase, respectively, as expected.

Because of these findings, we postulate the existence of a substrate-induced mechanistic switch from a DOT process involving *p*-$CNC_6H_4SCH_3$ to a proton-coupled ET process for *p*-$CH_3OC_6H_4SCH_3$, as shown in Fig. 7B. Within this hypothesis, in the latter case due to the acidity of the medium, the ET from the sulfide to $[N4Py{\cdot}Fe^{IV}(O)]^{2+}$ is coupled with a proton transfer to produce the sulfide radical cation *p*-$CH_3OC_6H_4SCH_3^{\bullet+}$ and the complex $[N4Py{\cdot}Fe^{III}(OH)]^{2+}$ (Fig. 7B). The fact that in the ms timescale we do not measure an appreciable contribution to the UV–Vis signal from *p*-$CH_3OC_6H_4SCH_3^{\bullet+}$, which is characterized by an intense absorption band centered at λ = 580 nm (ε = 7500 M^{-1} cm^{-1}),[75–78] may be ascribed to a fast competitive decay process of the radical cation due to a nucleophilic attack to the sulfur atom by AcOH and/or AcOOH (at the beginning of the reaction, the substrate, AcOOH and AcOH are approximately in a

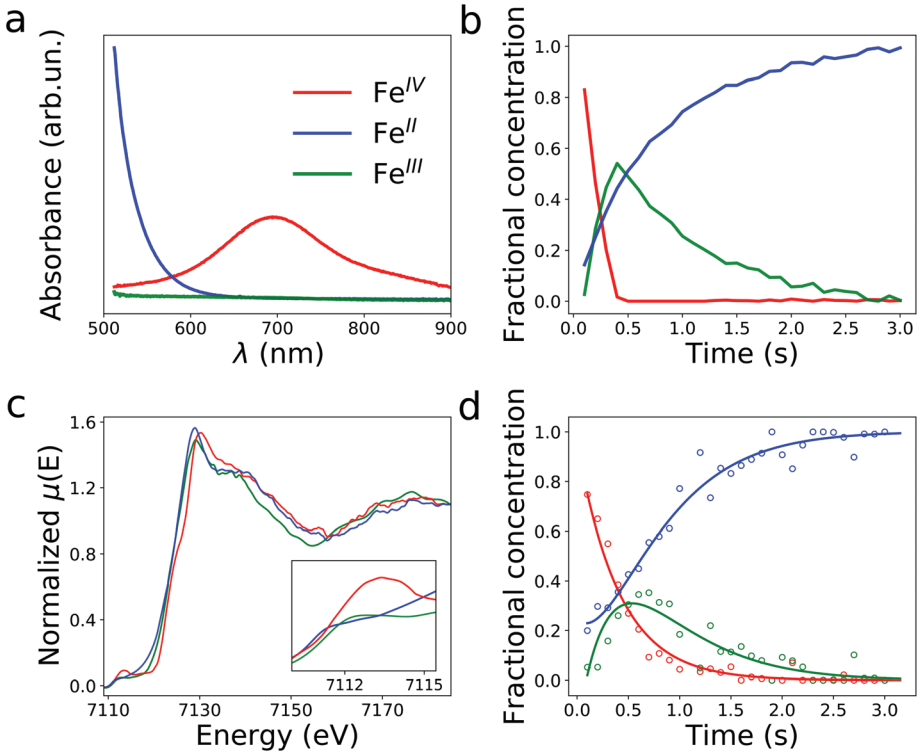

Fig. 6 Results of the decomposition of the spectroscopic data for the *p*-$CH_3OC_6H_4SCH_3$ oxidation. UV–Vis and Fe K-edge XANES extracted spectra assigned to the reaction key species (panels (a) and (c), respectively) and associated concentration profiles (panels (b) and (d), respectively). The dotted lines in panel (d) constitute the concentrations obtained through the decomposition of the EDXAS reaction data, while the full lines represent the best-fit analytical solutions to a $Fe^{IV} \overset{k_1}{\Rightarrow} Fe^{III} \overset{k_2}{\Rightarrow} Fe^{II}$ mechanistic scheme.

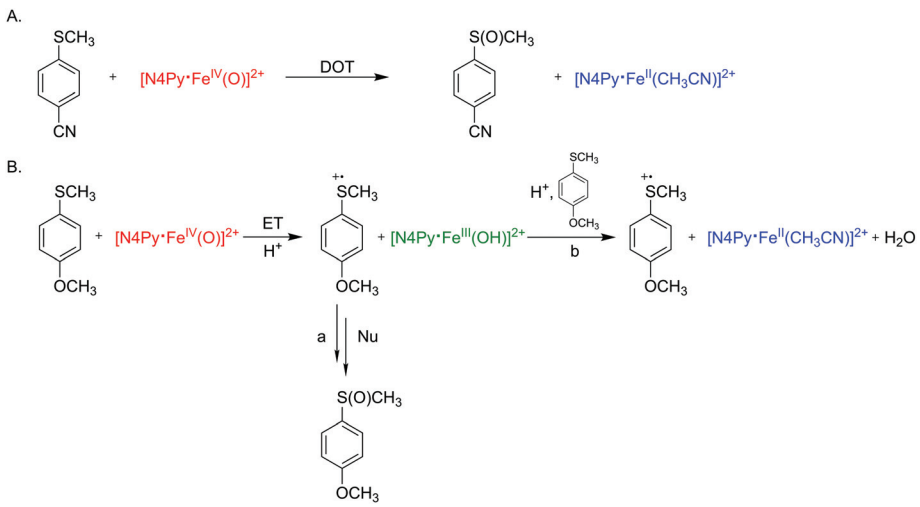

Fig. 7 Proposed mechanisms for the investigated reactions.

1.0 : 2.2 : 4.4 ratio) that prevents the radical cation accumulation (Fig. 7B, pathway a). This hypothesis is supported by the observation that the nucleophilic attack to the sulfur atom represents the main decay pathway of radical cations of aryl benzyl sulfides generated by anodic oxidation in AcOH leading to the corresponding sulfoxides.[79] Moreover, the relative contribution of this process increases in the presence of the electron donating aryl *p*-OCH_3 substituent. Under this hypothesis, the $[N4Py{\cdot}Fe^{III}(OH)]^{2+}$ species is stable enough to be detected in the ms timescale. Its decay to Fe^{II} is likely due to one-electron oxidation of another substrate molecule, which is present in large excess (Fig. 7B, pathway b). This reaction would be

favoured both by the acid environment that enhances the redox potential of the Fe^{III} species, and by the *para*-methoxy substituent, that makes the aryl sulfide a stronger reducing agent.

To verify the consistency of the matricial decomposition of the UV–Vis data relative to the *p*-$CH_3OC_6H_4SCH_3$ oxidation, the Savitzky–Golay smoothed EDXAS reaction data (presented in Fig. S1b†) were independently subjected to the matricial decomposition approach, in order to extract the three spectral and concentration profiles. The derived XANES spectra and fractional concentration profiles are presented in Fig. 6c and d. The threshold regions of all XANES spectra were analyzed to determine the energies of the main absorption edges, as previously outlined, and the results are shown in Fig. S5.† The XAS spectrum in blue was fixed to coincide with the EDXAS spectrum measured at t = 3.0 s from reaction start and it is assigned to complex $[N4Py{\cdot}Fe^{II}(CH_3CN)]^{2+}$. This assumption is motivated by the fact that the experimental XAS spectra and the energy positions of the main absorption edges show no variation after 3.0 s.[29] Moreover, the experimental XAS spectrum measured at 3.0 s has an edge position at 7124.7 eV and it is very similar to the XANES component of the Fe^{II} species extracted spectrum extracted from the *p*-$CNC_6H_4SCH_3$ reaction EDXAS data (Fig. 5c). The XANES components whose main absorption edges lie at the highest (red) and the intermediate (green) energies are assigned to complexes $[N4Py{\cdot}Fe^{IV}(O)]^{2+}$ and $[N4Py{\cdot}Fe^{III}(OH)]^{2+}$, respectively. In fact, the spectral components assigned to the Fe^{IV} and Fe^{III} species possess main absorption edge energy values of 7126.2 eV and of 7125.4 eV, respectively, as shown in Fig. S5a and S5b.† The edge energy of the Fe^{IV} complex is identical to that of the same species determined from the analysis of the *p*-$CNC_6H_4SCH_3$ reaction EDXAS data. The Fe^{III} complex possesses an intermediate main edge energy value if compared to those of the Fe^{IV} and Fe^{II} complexes as expected due to the intermediate oxidation state, similarly to complex $[N4Py{\cdot}Fe^{III}(OO^tBu)]^{2+}$,[66] as listed in Table S1.† The identification of the XANES spectra is strengthened by the presence of the characteristic 1s → 3d transition located at 7113.6(2) eV, 7112.4(2) eV and 7111.8(2) eV in the spectra assigned to the Fe^{IV}, Fe^{III} and Fe^{II} complexes, respectively (see inset of Fig. 6c). This feature is intense in the spectrum of the Fe^{IV} complex, less intense in that of the Fe^{III} species, and weak in that of the Fe^{II} compound, as previously reported for the same Fe^{IV} and Fe^{II} species and for the compound $[N4Py{\cdot}Fe^{III}(OO^tBu)]^{2+}$.[66] Additionally, the energy of the pre-edge peak of $[N4Py{\cdot}Fe^{III}(OH)]^{2+}$ is quite similar to those of other Fe^{III} high-valent complexes, such as $[Fe^{III}(CN)_6]^{3-}$ and $[Fe^{III}(prpep)_2]$ which are both equal to 7112.6 eV.[71]

The fractional concentration of the Fe^{IV} reactant rapidly decays to zero, while the concentration of the Fe^{II} species steadily increases, as expected for the reaction product. Conversely, the concentration of the Fe^{III} component increases to reach a maximum between t = 0.4 s and t = 0.8 s before reaching zero at t = 3.0 s. These results are in good agreement with the UV–Vis reaction monitoring of the decrease of the Fe^{IV} absorbance and the increase of the Fe^{II} absorbance shown in Fig. 3b and closely resemble the concentration profiles obtained by analyzing the UV–Vis data (Fig. 6b). The concentration profile trends shown in Fig. 6b and d show an evident level of similarity. The occurring differences can be attributed to the higher amount of noise affecting the XANES measurements and to a certain level of rotational ambiguity connected

Table 2 Best-fit nonstructural parameters obtained from the MXAN analysis of the Fe K-edge XANES spectra of the $[N4Py{\cdot}Fe^{IV}(O)]^{2+}$ (Fe^{IV}), $[N4Py{\cdot}Fe^{III}(OH)]^{2+}$ (Fe^{III}) and $[N4Py{\cdot}Fe^{II}(CH_3CN)]^{2+}$ (Fe^{II}) complexes. E_T is the difference between the theoretical threshold energy and the first inflection point of the XANES spectrum, E_F is the Fermi energy level, E_s and A_s are the energy and amplitude of the plasmon, Γ_{exp} is the experimental resolution

	E_T (eV)	E_F (eV)	Γ_{exp}	E_s (eV)	A_s	R_{sq}
Fe^{IV}	−3.7	−0.4	0.6	23.0	11.0	1.8[a]/2.5[b]
Fe^{III}	−4.8	4.6	0.7	25.3	7.1	1.7[a]
Fe^{II}	−5.7	1.37	0.6	28.5	12.4	1.5[a]/1.6[b]

[a] R_{sq} is the residual function for the *p*-$CH_3OC_6H_4SCH_3$ reaction. [b] R_{sq} is the residual function for the *p*-$CNC_6H_4SCH_3$ reaction.

Table 1 Best-fit structural parameters obtained from the analysis of the XANES spectra of the $[N4Py{\cdot}Fe^{IV}(O)]^{2+}$ (Fe^{IV}), $[N4Py{\cdot}Fe^{III}(OH)]^{2+}$ (Fe^{III}) and $[N4Py{\cdot}Fe^{II}(CH_3CN)]^{2+}$ (Fe^{II}) complexes, compared to the available literature crystallographic and EXAFS data. $R_{Fe-Namine}$ and R_{Fe-NPy} are the average distances between the metal cation, the single tertiary nitrogen atom and the four secondary nitrogen atoms of the N4Py molecule, respectively. $R_{Fe-NACN}$ is the distance between the metal cation and the nitrogen solvent atom. R_{Fe-O} is the distance between the metal cation and the coordinating oxygen atom, while N is the coordination number

	Fe–N_{amine}		Fe–N_{Py}		Fe–N_{ACN}		Fe–O	
	N	r (Å)	N	r (Å)	N	r (Å)	N	r (Å)
Fe^{IV}								
Cryst.[90]	1	2.033(8)	4	1.957(5)	—	—	1	1.639(5)
EXAFS[67]	—	—	4	1.96	—	—	1	1.64
This work	1	2.08(5)	4	2.00(5)	—	—	1	1.69(5)
Fe^{III}								
This work	1	1.97(5)	4	2.09(5)	—	—	1	1.89(5)
Fe^{II}								
Cryst.[91]	1	1.961(3)	4	1.967(3)–1.976(3)	1	1.915(3)	—	—
This work	1	2.01(5)	4	2.01(5)	1	1.96(5)	—	—

to the use of the transformation matrix approach, as described by Martini *et al.*[80]

By assuming a kinetic model for the reaction of the kind $Fe^{IV} \overset{k_1}{\Rightarrow} Fe^{III} \overset{k_2}{\Rightarrow} Fe^{II}$, the XAS-extracted concentration profiles were simultaneously fitted with the mathematical solutions to the differential equations describing the model (see eqn (10) of the ESI†). The results are shown in Fig. 6d (full lines) superimposed to the concentration profiles (dotted lines). The good agreement between the model and experimental concentration profiles ($R^2 = 0.985$) shows the versatility of our method, which may be applied also to suggest kinetic models of chemical reactions in solution occurring on the second to millisecond time scales.

In order to obtain structural information for all the reaction intermediates, a full multiple scattering (MS) analysis was carried out for the XANES spectra obtained for the isolated Fe species for both reactions.[81–89] The K-edge XANES spectra of the Fe^{IV} species are different from those of the Fe^{III} and Fe^{II}

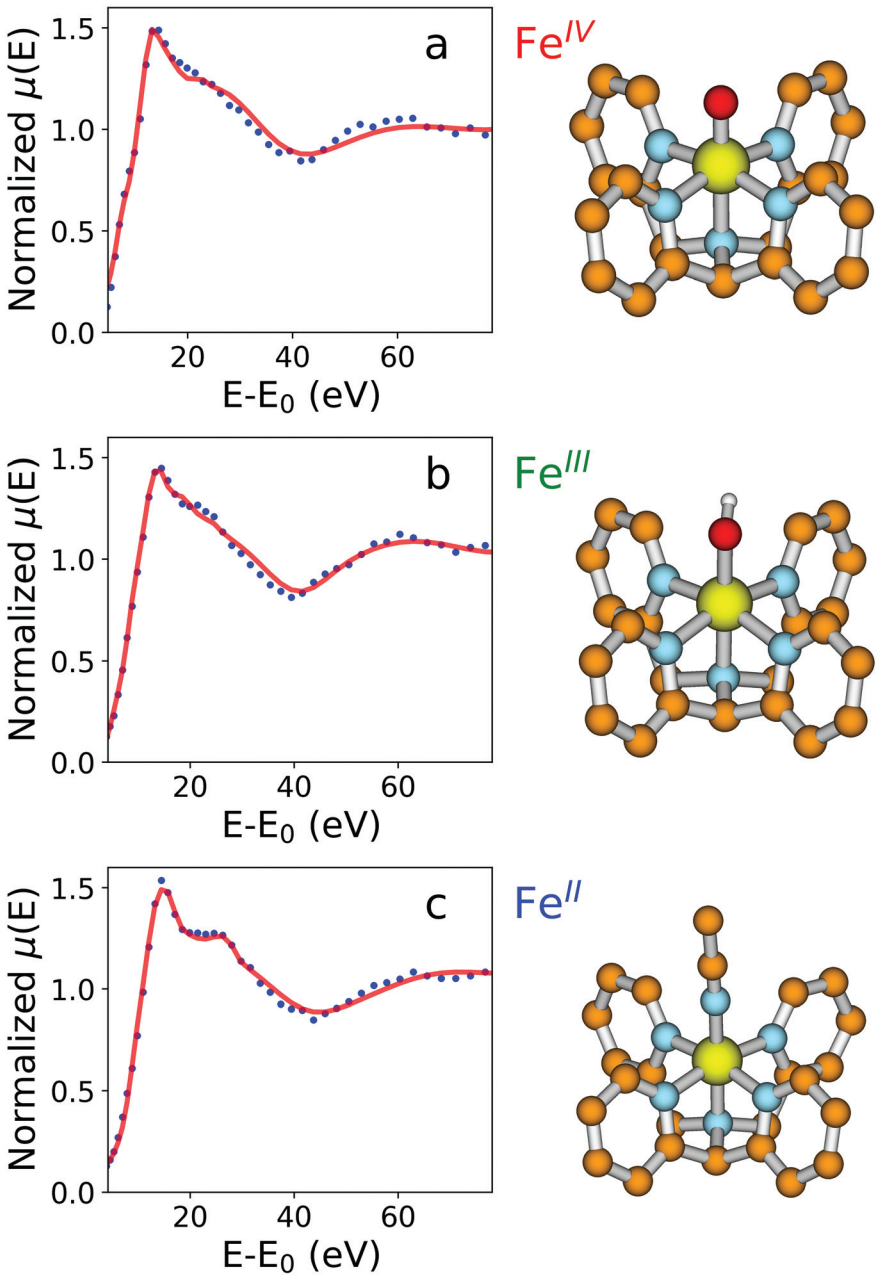

Fig. 8 Best-fit results for the Fe K-edge XANES spectral components extracted for the reaction between *p*-$CH_3OC_6H_4SCH_3$ and $[N4Py{\cdot}Fe^{IV}(O)]^{2+}$. The extracted XANES spectra (blue, dotted lines) are assigned to complexes $[N4Py{\cdot}Fe^{IV}(O)]^{2+}$ (a), $[N4Py{\cdot}Fe^{III}(OH)]^{2+}$ (b) and $[N4Py{\cdot}Fe^{II}(CH_3CN)]^{2+}$ (c) and compared to the theoretical curves (red, full lines) calculated with optimized geometrical models. The associated molecular clusters are also depicted, where iron, nitrogen, carbon, oxygen and hydrogen atoms are in yellow, cyan, orange, red and white, respectively.

complexes. In particular, the Fe^{IV} first coordination shell is made up by the five nitrogen atoms belonging to the N4Py ligand and one oxygen atom. A quantitative analysis of the XANES spectra has been carried out with the MXAN program starting from the crystallographic structure reported in ref. 90. A fitting procedure of the Fe^{IV} XANES extracted spectra has been performed by optimizing the nonstructural parameters while the Fe–N_{Py}, the Fe–N_{amine} and the Fe–O distances (see caption of Table 1) were allowed to vary within ±0.05 Å of the crystallographic ones. The best-fit results of the *p*-$CH_3OC_6H_4SCH_3$ and *p*-$CNC_6H_4SCH_3$ reactions are shown in Fig. 8a, and Fig. S6a,† respectively, along with the associated molecular clusters. The agreement between the theoretical and experimental data is very good and the same structural and nonstructural parameters have been obtained in both cases (see Tables 1 and 2).

As far as the Fe^{II} complex is concerned, the MXAN analyses have been conducted starting from the available crystallographic geometry.[91] In this structure, around the central Fe cation there are the five nitrogen atoms of the N4Py backbone and one nitrogen atom belonging to the CH_3CN solvent. Also in this case the minimization procedures were carried out allowing a variation of the Fe-ligand distances within ±0.05 Å of the crystal geometry. The results of the analyses are shown in Fig. 8c, and Fig. S6b† for the *p*-$CH_3OC_6H_4SCH_3$ and *p*-$CNC_6H_4SCH_3$ reactions, respectively. Also in this case the agreement between the experimental and theoretical spectra is excellent and the same structural and nonstructural parameters have been obtained in both cases (see Tables 1 and 2).

The XANES spectrum assigned to complex $[N4Py{\cdot}Fe^{III}(OH)]^{2+}$ was calculated starting from the crystallographic geometry of $[N4Py{\cdot}Fe^{IV}(O)]^{2+}$. The results of the analysis are shown in Fig. 8b where the experimental and theoretical curves are reported. Tables 1 and 2 list the associated structural and nonstructural parameters, respectively. One may note that for the Fe^{III} complex the Fe–N_{amine} and average Fe–N_{Py} distances are equal to 1.97(5) Å and 2.09(5) Å, respectively. The simulated Fe–O distance is 1.89(5) Å, a value quite different from the Fe–O distance of 1.69(5) Å evaluated in the case of the Fe^{IV} complex. These values are higher than the average Fe–N distance of 1.99 Å and the Fe–O distance of 1.81 Å determined for the Fe^{III}–OH intermediate by DFT-based calculations at the B3LYP/LACV3P^{*+}//LACVP level.[72] Further, in the crystal structure of complex $[N4Py{\cdot}Fe^{III}(OCH_3)]^{2+}$, where a methoxy group coordinates the iron site, the asymmetric unit possesses average Fe–N_{amine}, Fe–O and average Fe–N_{Py} distances of 2.149(3) Å, 1.780(3) Å and 2.08(2) Å, respectively.[92] These average Fe–N_{Py} distances closely resemble the average Fe–N_{Py} distance of 2.09(5) Å we have obtained in this investigation for the Fe^{III}–OH species. Recently, DFT calculations on the hydroxide complex $[Fe^{III}(OH)(N3PyO^{2Ph})]^{+}$, which shares many structural similarities with complex $[N4Py{\cdot}Fe^{III}(OH)]^{2+}$, led to an optimized geometry possessing a Fe–O distance of 1.96 Å.[93] Finally, in the crystal structure of complex $[Fe^{III}(OH)(N4Py^{2NpNH})][OTf]_2$ the Fe–O distance is equal to 1.837(3) Å.[94] It is of note that the Fe–N_{amine}, Fe–N_{Py} and Fe–O distances presented herein for complex $[N4Py{\cdot}Fe^{III}(OH)]^{2+}$ are identical within statistical errors to the distances evaluated for the same complex, as determined by a multivariate and theoretical analysis of EDXAS data for the oxidation of diphenylmethane by $[N4Py{\cdot}Fe^{IV}(O)]^{2+}$ in CH_3CN at room temperature and in the presence of AcOOH and AcOH. To the best of our knowledge, we present a first structural characterization of complex $[N4Py{\cdot}Fe^{III}(OH)]^{2+}$ in solution.

3. Conclusions

This work proves that it is possible to combine spectroscopic, statistical and theoretical techniques to study the mechanism of chemical reactions evolving in solution on the second to millisecond time scales and to obtain structural information on their relevant labile intermediates. To this end, we propose an innovative method that is based on the multivariate analysis of coupled EDXAS/UV–Vis spectra and on the subsequent quantitative analysis of the XANES spectra obtained for the reaction key components. The potentialities of this approach are demonstrated by its application to the sulfoxidation of *p*-cyanothioanisole and *p*-methoxythioanisole by the nonheme Fe^{IV} oxo complex $[N4Py{\cdot}Fe^{IV}(O)]^{2+}$. For these processes, we suggest that, in the presence of AcOOH and AcOH, $[N4Py{\cdot}Fe^{IV}(O)]^{2+}$ oxidizes *p*-$CH_3OC_6H_4SCH_3$ with a proton-coupled ET mechanism, as opposed to the DOT occurring in the *p*-$CNC_6H_4SCH_3$ oxidation. In the former reaction, we have clear evidence of the formation of $[N4Py{\cdot}Fe^{III}(OH)]^{2+}$ as a reaction intermediate. Notably, thanks to the employed strategy, the structures of all reaction intermediates are obtained. The proposed method may be of interest for the future investigation of complex chemical reactive pathways and for the quantitative description of their fleeting intermediates.

Conflicts of interest

There are no conflicts to declare.

Acknowledgements

The ESRF synchrotron radiation facility is acknowledged for the provision of beam time for time-resolved XAS (ID24). We acknowledge financial support from the Italian Ministry of University and Research (MIUR) through grant "PRIN 2017, 2017KKP5ZR, MOSCATo" and from University of Rome La Sapienza grant no. RG11916B702B43B9.

References

1 A. de Juan, M. Maeder, M. Martínez and R. Tauler, *Chemom. Intell. Lab. Syst.*, 2000, **54**, 123–141.
2 A. de Juan, M. Maeder, M. Martinez and R. Tauler, *Anal. Chim. Acta*, 2001, **442**, 337–350.

3 A. Abbaspour and M. Kamyabi, *Anal. Chim. Acta*, 2004, **512**, 257–269.
4 H. Abdollahi and V. Mahdavi, *Langmuir*, 2007, **23**, 2362–2368.
5 M. V. Bosco and M. S. Larrechi, *Talanta*, 2007, **71**, 1703–1709.
6 M. Bosco, M. Callao and M. Larrechi, *Talanta*, 2007, **72**, 800–807.
7 R. Gargallo, M. Vives, R. Tauler and R. Eritja, *Biophys. J.*, 2001, **81**, 2886–2896.
8 M. Vives, R. Gargallo, R. Tauler and V. Moreno, *J. Inorg. Biochem.*, 2001, **85**, 279–290.
9 M. Vives, R. Tauler, V. Moreno and R. Gargallo, *Anal. Chim. Acta*, 2001, **446**, 437–448.
10 J. Jaumot, V. Marchán, R. Gargallo, A. Grandas and R. Tauler, *Anal. Chem.*, 2004, **76**, 7094–7101.
11 A. Borges, R. Tauler and A. de Juan, *Anal. Chim. Acta*, 2005, **544**, 159–166.
12 B. Czarnik-Matusewicz and S. Pilorz, *J. Mol. Struct.*, 2006, **799**, 211–220.
13 M. Blanco, A. Peinado and J. Mas, *Anal. Chim. Acta*, 2005, **544**, 199–205.
14 S. Šašić, Y. Ozaki, A. Olinga and H. Siesler, *Anal. Chim. Acta*, 2002, **452**, 265–276.
15 M. Garrido, I. Lázaro, M. Larrechi and F. Rius, *Anal. Chim. Acta*, 2004, **515**, 65–73.
16 J. Diewok, M. J. Ayora-Cañada and B. Lendl, *Anal. Chem.*, 2002, **74**, 4944–4954.
17 J. Diewok, A. de Juan, M. Maeder, R. Tauler and B. Lendl, *Anal. Chem.*, 2003, **75**, 641–647.
18 M. López-Pastor, M. J. Ayora-Cañada, M. Valcárcel and B. Lendl, *J. Phys. Chem. B*, 2006, **110**, 10896–10902.
19 C. Ruckebusch, L. Duponchel, B. Sombret, J. P. Huvenne and J. Saurina, *J. Chem. Inf. Comput. Sci.*, 2003, **43**, 1966–1973.
20 C. Ruckebusch, L. Duponchel, J.-P. Huvenne and J. Saurina, *Vib. Spectrosc.*, 2004, **35**, 21–26.
21 N. Kaun, M. J. Vellekoop and B. Lendl, *Appl. Spectrosc.*, 2006, **60**, 1273–1278.
22 M. López-Pastor, A. Domínguez-Vidal, M. J. Ayora-Cañada, M. Valcárcel and B. Lendl, *J. Mol. Struct.*, 2006, **799**, 146–152.
23 B. Muik, B. Lendl, A. Molina-Diaz, M. Valcarcel and M. J. Ayora-Cañada, *Anal. Chim. Acta*, 2007, **593**, 54–67.
24 M. B. B. Abdul Rahman, P. R. Bolton, J. Evans, A. J. Dent, I. Harvey and S. Diaz-Moreno, *Faraday Discuss.*, 2003, **122**, 211–222.
25 G. Guilera, M. A. Newton, C. Polli, S. Pascarelli, M. Guinó and K. K. M. Hii, *Chem. Commun.*, 2006, 4306–4308.
26 F. Tavani, A. Martini, F. Sessa, G. Olivo, G. Capocasa, O. Lanzalunga, S. Di Stefano and P. D'Angelo, *J. Phys.: Conf. Ser.*, 2021, accepted.
27 P. D'Angelo, G. Chillemi, V. Barone, G. Mancini, N. Sanna and I. Persson, *J. Phys. Chem. B*, 2005, **109**, 9178–9185.
28 G. Olivo, A. Barbieri, V. Dantignana, F. Sessa, V. Migliorati, M. Monte, S. Pascarelli, T. Narayanan, O. Lanzalunga, S. Di Stefano and P. D'Angelo, *J. Phys. Chem. Lett.*, 2017, **8**, 2958–2963.
29 G. Capocasa, F. Sessa, F. Tavani, M. Monte, G. Olivo, S. Pascarelli, O. Lanzalunga, S. Di Stefano and P. D'Angelo, *J. Am. Chem. Soc.*, 2019, **141**, 2299–2304.
30 A. I. Frenkel, O. Kleifeld, S. R. Wasserman and I. Sagi, *J. Chem. Phys.*, 2002, **116**, 9449–9456.
31 O. Kleifeld, A. I. Frenkel, J. Martin and I. Sagi, *Nat. Struct. Mol. Biol.*, 2003, **10**, 98–103.
32 A. Solomon, B. Akabayov, A. Frenkel, M. E. Milla and I. Sagi, *Proc. Natl. Acad. Sci. U. S. A.*, 2007, **104**, 4931–4936.
33 Q. Wang, J. C. Hanson and A. I. Frenkel, *J. Chem. Phys.*, 2008, **129**, 234502.
34 G. Smolentsev, G. Guilera, M. Tromp, S. Pascarelli and A. V. Soldatov, *J. Chem. Phys.*, 2009, **130**, 174508.
35 B. L. Caetano, V. Briois, S. H. Pulcinelli, F. Meneau and C. V. Santilli, *J. Phys. Chem. C*, 2017, **121**, 886–895.
36 H. W. Carvalho, S. H. Pulcinelli, C. V. Santilli, F. Leroux, F. Meneau and V. Briois, *Chem. Mater.*, 2013, **25**, 2855–2867.
37 A. Martini, E. Alladio and E. Borfecchia, *Top. Catal.*, 2013, **61**, 1296–1407.
38 A. Martini, E. Borfecchia, K. A. Lomachenko, I. A. Pankin, C. Negri, G. Berlier, P. Beato, H. Falsig, S. Bordiga and C. Lamberti, *Chem. Sci.*, 2017, **8**, 6836–6851.
39 A. Voronov, A. Urakawa, W. van Beek, N. E. Tsakoumis, H. Emerich and M. R, *Anal. Chim. Acta*, 2014, **840**, 20–27.
40 W. H. Cassinelli, L. Martins, A. R. Passos, S. H. Pulcinelli, C. V. Santilli, A. Rochet and V. Briois, *Catal. Today*, 2014, **229**, 114–122.
41 A. Rochet, B. Baubet, V. Moizan, C. Pichon and V. Briois, *C. R. Chim.*, 2016, **19**, 1337–1351.
42 A. Rochet, B. Baubet, V. Moizan, E. Devers, A. Hugon, C. Pichon, E. Payen and V. Briois, *J. Phys. Chem. C*, 2017, **121**, 18544–18556.
43 P. Conti, S. Zamponi, M. Giorgetti, M. Berrettoni and W. H. Smyrl, *Anal. Chem.*, 2010, **82**, 3629–3635.
44 M. Fernandez-Garcia, C. Marquez Alvarez and G. L. Haller, *J. Phys. Chem.*, 1995, **99**, 12565–12569.
45 A. Martini, S. Guda, A. Guda, G. Smolentsev, A. Algasov, O. Usoltsev, M. Soldatov, A. Bugaev, Y. Rusalev, C. Lamberti and A. Soldatov, *Comput. Phys. Commun.*, 2019, 107064.
46 F. Tavani, A. Martini, G. Capocasa, S. Di Stefano, O. Lanzalunga and P. D'Angelo, *Inorg. Chem.*, 2020, **59**, 9979–9989.
47 J. Park, Y. Morimoto, Y.-M. Lee, W. Nam and S. Fukuzumi, *J. Am. Chem. Soc.*, 2011, **133**, 5236–5239.
48 Y. Goto, T. Matsui, S. Ozaki, Y. Watanabe and S. Fukuzumi, *J. Am. Chem. Soc.*, 1999, **121**, 9497–9502.
49 B. Meunier, S. P. de Visser and S. Shaik, *Chem. Rev.*, 2004, **104**, 3947–3980.
50 C. Krebs, D. G. Fujimori, C. T. Walsh and J. M. Bollinger, *Acc. Chem. Res.*, 2007, **40**, 484–492.
51 W. Nam, *Acc. Chem. Res.*, 2007, **40**, 522–531.
52 J. Arias, C. R. Newlands and M. M. Abu-Omar, *Inorg. Chem.*, 2001, **40**, 2185–2192.

53 A. Kumar, I. Goldberg, M. Botoshansky, Y. Buchman and Z. Gross, *J. Am. Chem. Soc.*, 2010, **132**, 15233–15245.
54 E. Baciocchi, M. F. Gerini, O. Lanzalunga, A. Lapi and M. Grazia Lo Piparo, *Org. Biomol. Chem.*, 2003, **1**, 422–426.
55 J. Park, Y. Morimoto, Y.-M. Lee, W. Nam and S. Fukuzumi, *J. Am. Chem. Soc.*, 2012, **134**, 3903–3911.
56 Y. Morimoto, H. Kotani, J. Park, Y.-M. Lee, W. Nam and S. Fukuzumi, *J. Am. Chem. Soc.*, 2011, **133**, 403–405.
57 J. Park, Y. Morimoto, Y.-M. Lee, W. Nam and S. Fukuzumi, *Inorg. Chem.*, 2014, **53**, 3618–3628.
58 A. Barbieri, S. D. Stefano, O. Lanzalunga, A. Lapi, M. Mazzonna and G. Olivo, *Phosphorus, Sulfur Silicon Relat. Elem.*, 2017, **192**, 241–244.
59 A. Barbieri, T. Del Giacco, S. Di Stefano, O. Lanzalunga, A. Lapi, M. Mazzonna and G. Olivo, *J. Org. Chem.*, 2016, **81**, 12382–12387.
60 A. Barbieri, R. De Carlo Chimienti, T. Del Giacco, S. Di Stefano, O. Lanzalunga, A. Lapi, M. Mazzonna, G. Olivo and M. Salamone, *J. Org. Chem.*, 2016, **81**, 2513–2520.
61 E. Baciocchi, M. Bettoni, O. Lanzalunga, M. Mazzonna and P. Mencarelli, *J. Org. Chem.*, 2011, **76**, 573–582.
62 T. Del Giacco, O. Lanzalunga, M. Mazzonna and P. Mencarelli, *J. Org. Chem.*, 2012, **77**, 1843–1852.
63 In the case of *p*-CNC_6H_4SMe a k_2 of 0.044 M^{-1} s^{-1} is reported in ref. 55 which corresponds to $k = k_2 \times$ [substrate] = 0.04 s^{-1} in our experimental conditions. By following the shift in time of the energy position of the main absorption edge we have measured a k value of 0.08 ± 0.04 s^{-1} for the process.[29].
64 P. A. Gorry, *Anal. Chem.*, 1990, **62**, 570–573.
65 C. Ruckebusch and L. Blanchet, *Anal. Chim. Acta*, 2013, **765**, 28–36.
66 J.-U. Rohde, S. Torelli, X. Shan, M. H. Lim, E. J. Klinker, J. Kaizer, K. Chen, W. Nam and L. Que, *J. Am. Chem. Soc.*, 2004, **126**, 16750–16761.
67 D. Wang, K. Ray, M. J. Collins, E. R. Farquhar, J. R. Frisch, L. Gómez, T. A. Jackson, M. Kerscher, A. Waleska, P. Comba, M. Costas and L. Que, *Chem. Sci.*, 2013, **4**, 282–291.
68 J.-U. Rohde, S. Torelli, X. Shan, M. H. Lim, E. J. Klinker, J. Kaizer, K. Chen, W. Nam and L. Que, *J. Am. Chem. Soc.*, 2004, **126**, 16750–16761.
69 S. DeBeer George, T. Petrenko and F. Neese, *J. Phys. Chem. A*, 2008, **112**, 12936–12943.
70 M. Lundberg, T. Kroll, S. DeBeer, U. Bergmann, S. A. Wilson, P. Glatzel, D. Nordlund, B. Hedman, K. O. Hodgson and E. I. Solomon, *J. Am. Chem. Soc.*, 2013, **135**, 17121–17134.
71 P. Chandrasekaran, S. C. E. Stieber, T. J. Collins, L. Que Jr., F. Neese and S. DeBeer, *Dalton Trans.*, 2011, **40**, 11070–11079.
72 K.-B. Cho, X. Wu, Y.-M. Lee, Y. H. Kwon, S. Shaik and W. Nam, *J. Am. Chem. Soc.*, 2012, **134**, 20222–20225.
73 Y. Nishida, Y. Morimoto, Y.-M. Lee, W. Nam and S. Fukuzumi, *Inorg. Chem.*, 2013, **52**, 3094–3101.
74 A. Martini and E. Borfecchia, *Crystals*, 2020, **10**, 664.
75 M. Ioele, S. Steenken and E. Baciocchi, *J. Phys. Chem. A*, 1997, **101**, 2979–2987.
76 S. Tojo, M. Fujitsuka and T. Majima, *RSC Adv.*, 2016, **6**, 109334–109339.
77 O. Lanzalunga and A. Lapi, *J. Sulfur. Chem.*, 2012, **33**, 101–129.
78 M. Jonsson, J. Lind, G. Merényi and T. E. Eriksen, *J. Chem. Soc., Perkin Trans. 2*, 1995, 67–70.
79 E. Baciocchi, C. Rol, E. Scamosci and G. V. Sebastiani, *J. Org. Chem.*, 1991, **56**, 5498–5502.
80 A. Martini, A. A. Guda, S. A. Guda, A. Dulina, F. Tavani, P. D'Angelo, E. Borfecchia and A. Soldatov, *J. Phys.: Conf. Ser.*, 2021, accepted.
81 M. Benfatto and S. Della Longa, *J. Synchrotron Radiat.*, 2001, **8**, 1087–1094.
82 M. Benfatto, S. Della Longa and C. R. Natoli, *J. Synchrotron Radiat.*, 2003, **10**, 51–57.
83 P. D'Angelo, A. Zitolo, G. Aquilanti and V. Migliorati, *J. Phys. Chem. B*, 2013, **117**, 12516–12524.
84 E. Burattini, P. D'Angelo, A. Di Cicco, A. Filipponi and N. V. Pavel, *J. Phys. Chem.*, 1993, **97**, 5486–5494.
85 K. Hayakawa, K. Hatada, P. D'Angelo, S. Della Longa, C. Natoli and M. Benfatto, *J. Am. Chem. Soc.*, 2005, **126**, 15618–15623.
86 P. D'Angelo, A. Lapi, V. Migliorati, A. Arcovito, M. Benfatto, O. M. Roscioni, W. Meyer-Klaucke and S. Della Longa, *Inorg. Chem.*, 2008, **47**, 9905–9918.
87 G. Salzano, M. Brennich, G. Mancini, T. Tran, G. Legname, P. D'Angelo and G. Giachin, *Biophys. J.*, 2020, **118**, 676–687.
88 A. Arcovito, T. Moschetti, P. D'Angelo, G. Mancini, B. Vallone, M. Brunori and S. Della Longa, *Arch. Biochem. Biophys.*, 2008, **475**, 7–13.
89 P. D'Angelo, V. Migliorati, F. Sessa, G. Mancini and I. Persson, *J. Phys. Chem. B*, 2016, **120**, 4114–4124.
90 E. J. Klinker, J. Kaizer, W. W. Brennessel, N. L. Woodrum, C. J. Cramer and L. Que Jr., *Angew. Chem., Int. Ed.*, 2005, **44**, 3690–3694.
91 G. Roelfes, M. Lubben, K. Chen, R. Y. N. Ho, A. Meetsma, S. Genseberger, R. M. Hermant, R. Hage, S. K. Mandal, V. G. Young, Y. Zang, H. Kooijman, A. L. Spek, L. Que and B. L. Feringa, *Inorg. Chem.*, 1999, **38**, 1929–1936.
92 G. Roelfes, M. Lubben, K. Chen, R. Y. N. Ho, A. Meetsma, S. Genseberger, R. M. Hermant, R. Hage, S. K. Mandal, V. G. Young, Y. Zang, H. Kooijman, A. L. Spek, L. Que and B. L. Feringa, *Inorg. Chem.*, 1999, **38**, 1929–1936.
93 T. M. Pangia, V. Yadav, E. F. Gérard, Y.-T. Lin, S. P. de Visser, G. N. L. Jameson and D. P. Goldberg, *Inorg. Chem.*, 2019, **58**, 9557–9561.
94 H. S. Soo, A. C. Komor, A. T. Iavarone and C. J. Chang, *Inorg. Chem.*, 2009, **48**, 10024–10035.